optica

Topological phase transition in an all-optical exciton-polariton lattice

Maciej Pieczarka,[1,2,8] Eliezer Estrecho,[1] Sanjib Ghosh,[3] Matthias Wurdack,[1] Mark Steger,[4,5] David W. Snoke,[4] Kenneth West,[6] Loren N. Pfeiffer,[6] Timothy C. H. Liew,[3] Andrew G. Truscott,[7] and Elena A. Ostrovskaya[1,9]

[1]ARC Centre of Excellence in Future Low-Energy Electronics Technologies and Nonlinear Physics Centre, Research School of Physics, The Australian National University, Canberra, ACT 2601, Australia
[2]Department of Experimental Physics, Faculty of Fundamental Problems of Technology, Wrocław University of Science and Technology, Wyb. Wyspiańskiego 27, 50-370 Wrocław, Poland
[3]Division of Physics and Applied Physics, School of Physical and Mathematical Sciences, Nanyang Technological University, Singapore 637371, Singapore
[4]Department of Physics and Astronomy, University of Pittsburgh, Pittsburgh, Pennsylvania 15260, USA
[5]Current address: National Renewable Energy Laboratory, Golden, Colorado 80401, USA
[6]Department of Electrical Engineering, Princeton University, Princeton, New Jersey 08544, USA
[7]Laser Physics Centre, Research School of Physics, The Australian National University, Canberra, ACT 2601, Australia
[8]e-mail: maciej.pieczarka@pwr.edu.pl
[9]e-mail: elena.ostrovskaya@anu.edu.au

Received 5 April 2021; revised 12 July 2021; accepted 12 July 2021 (Doc. ID 426996); published 11 August 2021

Topological insulators are a class of electronic materials exhibiting robust edge states immune to perturbations and disorder. This concept has been successfully adapted in photonics, where topologically nontrivial waveguides and topological lasers were developed. However, the exploration of topological properties in a given photonic system is limited to a fabricated sample, without the flexibility to reconfigure the structure *in situ*. Here, we demonstrate an all-optical realization of the orbital Su–Schrieffer–Heeger model in a microcavity exciton-polariton system, whereby a cavity photon is hybridized with an exciton in a GaAs quantum well. We induce a zigzag potential for exciton polaritons all-optically by shaping the nonresonant laser excitation, and measure directly the eigenspectrum and topological edge states of a polariton lattice in a nonlinear regime of bosonic condensation. Furthermore, taking advantage of the tunability of the optically induced lattice, we modify the intersite tunneling to realize a topological phase transition to a trivial state. Our results open the way to study topological phase transitions on-demand in fully reconfigurable hybrid photonic systems that do not require sophisticated sample engineering.

https://doi.org/10.1364/OPTICA.426996

1. INTRODUCTION

Microcavity exciton polaritons (polaritons therein), hybrid quasiparticles resulting from strong coupling of excitons and photons in a semiconductor microcavity [1–4], have emerged as a perfect platform for numerous applications in nonlinear and topological photonics [5–12]. These interacting bosons combine a very low effective mass inherited from cavity photons with repulsive interactions inherited from excitons, allowing for bosonic condensation at elevated temperatures.

Taking advantage of the photonic part of a polariton, one can modify the planar microcavity by various fabrication techniques and realize polariton trapping potentials, as well as a lattice of coupled traps [10,13–15]. Additionally, the TE-TM polarized modes splitting in a planar cavity results in an effective spin–orbit interaction for polaritons enabling realizations of topological and flatband systems [10,14,16,17]. Nevertheless, this technological approach has a major practical drawback, as once the sample is made, there is little or no room for modification of its properties. This limits the applications of polariton-based photonic topological devices, where active control is highly desirable [18–21].

One of the possible ways to achieve active control is to use surface acoustic waves, which simultaneously affect the cavity and exciton energies [22,23]. Alternatively, only the excitonic component of the polariton can be used for engineering the trapping potential. Under nonresonant optical excitation above the semiconductor material bandgap, the pumping laser creates a high-energy excitonic reservoir [24], which acts as a non-Hermitian potential that replenishes and repels polaritons due to exciton-polariton interactions [13,25–27]. The excitonic potential can therefore be shaped by a spatially structured laser excitation.

In this work, we employ a spatially structured laser beam, imaged via a microscope objective onto a planar microcavity

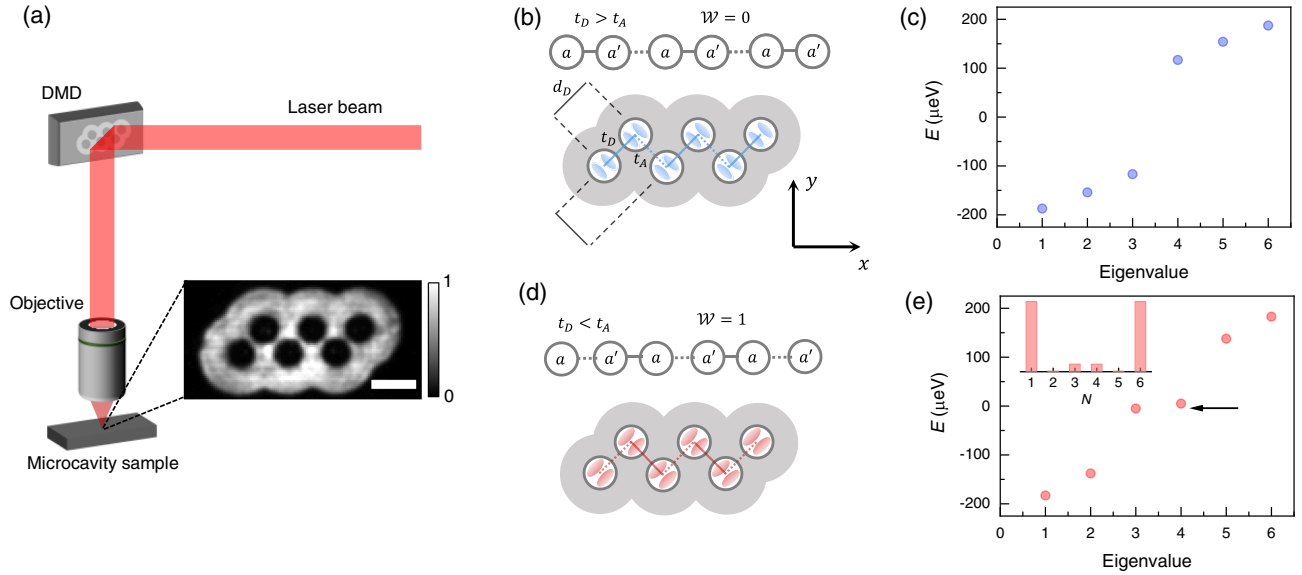

Fig. 1. Realization of an orbital SSH Hamiltonian with a nonresonant optical excitation. (a) Simplified scheme of the experimental setup for creating exciton polaritons in an optically induced trapping potential. Inset presents the spatial distribution of the laser pump reflected from the sample. Dark areas correspond to polariton traps with the trap diameter $D_{trap} \approx 5.9$ μm, arranged in a zigzag chain. White scale bar corresponds to 10 μm. (b), (d) Sketch of the orbital SSH model for (b) topologically trivial and (d) nontrivial cases, realized with the trapped p-modes of different orientations A, D. (c), (e) Eigenenergies of a tight-binding Hamiltonian model corresponding to the $N = 6$ chain in (b), (d). Edge states within the gap are indicated with an arrow in (e). Inset shows the probability density distribution of the edge state.

sample with embedded GaAs quantum wells (QWs) [see Fig. 1(a)]. Spatial structuring is achieved by selectively reflecting the laser beam from a programmed digital micromirror device (DMD) (see Methods, Section 2.A, for details). The spatial distribution of the pump effectively creates a chain of coupled circular traps in zigzag geometry, first proposed for realization of low-dimensional topological systems in plasmonics and nanophotonics [28–33]. Exciton polaritons trapped in this optically induced chain realize the orbital version of the Su–Schrieffer–Heeger (SSH) model, previously demonstrated in etched samples with coupled micropillars [14,15,34]. We note that an all-optical linear SSH chain [35], with alternating separation between the lattice sites, was recently created in the configuration of ballistically expanding condensates from tightly focused excitation spots [17,36]. However, the band structure analysis is very challenging in this configuration due to complexity of the data, where the condensate is expanding in all directions, preventing observation of topologically nontrivial edge modes. We address these challenges by optically trapping [25,37,38] the polaritons that naturally separate the condensate from the reservoir. This is enabled by the efficient energy relaxation in our samples [38], where the condensate forms in the lowest-energy states of the trap instead of ballistically expanding. We demonstrate the topological phase transition using a zigzag chain of optically trapped polariton condensates, as described below.

The SSH chain [39] is the simplest realization of a topological insulator in one dimension. Here, we focus on the SSH model realized with the p-modes of each circular trap, coupled as shown in Figs. 1(b) and 1(d). In contrast to linear chains with alternating distances between the lattice sites [35,40,41], the orthogonality of the p-modes makes the SSH model valid for $d_A = d_D = d$, where d_A and d_D are the lattice constants in the antidiagonal (A) and diagonal (D) directions [15]. This is because the tunneling amplitudes in these two directions, t_A and t_D, are different due to the collinear or orthogonal alignment of the p-modes with the axis linking the consecutive traps. As a result, two configurations exist in finite length chains with an even number of lattice sites, with the staggering order being trivial $t_D > t_A$ for diagonal, p_D, and nontrivial $t_D < t_A$ for antidiagonal, p_A, mode orientations. The two different configurations (phases) are presented in Figs. 1(b) and 1(d). They are characterized by the phase winding numbers $\mathcal{W} = 0$ for trivial and $\mathcal{W} = 1$ for topological phase (see Methods, Section 2.B). The eigenenergies of a tight binding Hamiltonian model, Eq. (1) for finite sized chains investigated in this work, are presented in Figs. 1(c) and 1(e). The normal phase in Fig. 1(c) is characterized by a spectrum with a trivial bandgap. The topologically nontrivial phase, presented in Fig. 1(e), differs from Fig. 1(c), as two eigenvalues close to zero energy emerge in the bandgap. The corresponding eigenstates are strongly localized at the edges of the chain [see inset in Fig. 1(e)] and are an indicator of a topological phase. In short chains, the spectra are discrete, and the edge states can have energies slightly different from zero, depending on the ratio of the tunneling amplitudes t_D/t_A. Nevertheless, the topological properties of the system are maintained.

2. METHODS

A. Sample and Experiment

The sample used in the experiment is a high-quality GaAs-based microcavity with a long cavity photon lifetime exceeding 100 ps [42,43]. The cavity of length $3\lambda/2$ is enclosed between distributed Bragg reflectors with 32 (top) and 40 (bottom) $Al_{0.2}Ga_{0.8}As/AlAs$ layer pairs. The active region is made of 12 GaAs/AlAs QWs of 7 nm nominal thickness positioned in three groups at the maxima of the confined photon field. The measured Rabi splitting is about $\hbar\Omega = 15.9 \pm 0.1$ meV. The experiments are done at slightly varying positions on the sample that correspond to the same photon–exciton detuning $\Delta = -0.43$ meV. All results are

obtained with a microcavity kept in a continuous-flow helium cryostat, ensuring a sample temperature of 7 –8 K.

The nonresonant optical excitation was provided by a continuous-wave (CW) Ti:sapphire laser (M Squared SolsTiS), tuned to the cavity reflectivity minimum above the QW bandgap. The Gaussian laser beam was transformed and focused to a top-hat distribution by a shaping lens (Eksma Optics GTH-5-250-4) and imaged onto the DMD. The shape of the lattice potential was encoded on the DMD. which reflected the laser selectively, and then imaged onto the sample via a set of lenses and a microscope objective (numerical aperture NA = 0.5) [26] [see Fig. 1(a)]. Photoluminescence from the sample was collected with the same objective in reflection geometry and imaged with a set of confocal lenses onto the slit of the spectrometer (Princeton Instruments IsoPlane 320), equipped with a 2D sensitive CCD (Andor iXon Ultra 888). The linewidth spectral resolution limit of the setup was measured to be about 60 μeV. The imaging lens in front of the spectrometer was mounted on a motorized stage, enabling the spectral tomography of the emission. The tomography was done by collecting a set of spectral images, scanning the full real-space emission by moving the image with respect to the entrance slit. The step of the tomographical scan results in resolution in the vertical direction of the images of about $\Delta y \approx 0.25$ μm, whereas the resolution in the horizontal axis is set by the camera pixel size, and it yields $\Delta x \approx 0.35$ μm.

The current experimental configuration is limited by the total output power of the pumping laser. Generation of SSH chains that are longer than those presented here is possible with higher pumping power to maintain the same peak intensity on the sample.

B. Theory

The SSH model is described by a tight-binding Hamiltonian:

$$\hat{H}_{SSH} = \sum_i \left(t_D \hat{a}_i^\dagger \hat{a}_i' + t_A \hat{a}_{i+1}^\dagger \hat{a}_i' + \text{h.c.} \right), \tag{1}$$

where $\hat{a}_i$ and $\hat{a}_i'$ are the annihilation operators in the ith unit cell of a lattice. The eigenfunctions of the Hamiltonian $\hat{H}_{SSH}$ are given by $(\pm e^{-i\varphi(k)}, 1)$, with k being the wave vector. The winding number $\mathcal{W}$ is defined by

$$\mathcal{W} = \frac{1}{2\pi} \int_{\text{BZ}} \mathrm{d}k, \quad \frac{\partial \varphi(k)}{\partial k}, \tag{2}$$

corresponding to the Zak phase $\mathcal{Z} = \pi \mathcal{W}$, which is a 1D lattice equivalent of the geometric Berry phase. In an ideal SSH model, $\mathcal{W} = 1$ for $t_D < t_A$ and $\mathcal{W} = 0$ for $t_D > t_A$. In our system, the lattice is perturbed by a potential gradient and disorder. To include these effects, we consider a Hamiltonian given by

$$\hat{H} = \hat{H}_{SSH} + \sum_i \left(V_{2i-1} \hat{a}_i^\dagger \hat{a}_i + V_{2i} \hat{a}_i'^\dagger \hat{a}_i' \right). \tag{3}$$

The potential energy is given by $V_i = v_i + v_0(i - N/2)$, where v_0 is a constant, v_i is a random value representing disorder in the system, and N is the number of unit cells in the lattice. For our simulations $v_0 = 0.2/N$, v_i is randomly distributed within the interval $[\pm 0.05]$, and energies are expressed in the unit of $\max(t_A, t_D)$.

Within the mean-field approximation, exciton polaritons in optically induced potentials can be described by a driven-dissipative equation for the polariton wavefunction, $\psi(x, y, t)$:

$$i\hbar \frac{\partial \psi}{\partial t} = \left[-\lambda \frac{\hbar^2}{2m} \nabla^2 + iP + V(x, y) + \alpha |\psi|^2 \right] \psi, \tag{4}$$

where $\lambda = (1 - i\lambda_0)$, λ_0 is a phenomenological parameter describing the energy relaxation [44], and m is the effective mass of the polaritons. The net gain $P(x, y) = P_0(x, y) - \gamma$ is given by the difference between the pump strength (gain) $P_0(x, y)$ and the loss γ (linewidth). The parameter $\alpha = (\alpha_R - i\alpha_I)$ represents the polariton–polariton interaction α_R and nonlinear decay α_I. $V(x, y)$ accounts for a real part of the potential (SSH lattice) induced by the repulsive interactions of the polaritons with an optically injected excitonic reservoir, as well as for the energy gradient in the cavity. For numerical simulations, we consider $\alpha_R = \alpha_I$ and a transformation $\psi \to \psi/\sqrt{\alpha_R}$ to obtain an equation describing the exciton polaritons: $i\hbar \partial\psi/\partial t = [-(\lambda\hbar^2)/(2m)\nabla^2 + iP(x, y) + V(x, y) + (1 - 1i)|\psi|^2]\psi$. The assumption on α_I is for convenience, as the particular choice of this value determines the overall losses, which result in a lower amplitude of the calculated field. Hence, the change of α_I does not affect the qualitative result of the simulation at a given pump strength P_0. The loss and effective mass parameters are obtained from the experimental data in [42,43]. Considering the long lifetime of exciton polaritons in our GaAs-based sample, we use a linewidth $\gamma = 5.5$ μeV corresponding to a lifetime of 120 ps. We take $m = 7.6 \times 10^{-5}\ \mathrm{m}_e$, where m_e is the mass of an electron. Other parameters were chosen as $\lambda_0 = 0.05$ meV and $\max(P_0) = 10.5$ μeV, to fit the phenomenology of the present experiment.

3. RESULTS

We investigate the optically induced SSH chain at pump powers slightly above and well above the exciton-polariton condensation threshold [see Figs. 2(a) and 2(b)]. The narrowing of the linewidth of the exciton-polariton emission above the condensation threshold allows us to resolve the ground and excited bands with the corresponding bandgaps [Fig. 2(c)]. The low-energy s-band is highly populated due to efficient energy relaxation of polaritons towards the ground state [45]. This is in contrast to the observation in [35], where the condensate is formed in higher bands. We also observe nonzero occupation of excited states forming a higher-energy band [Figs. 2(c) and 2(d)].

The corresponding position-resolved spectrum at pumping power $P_0 \approx 24.3$ mW is presented in Fig. 3(a). The intense signal from the s-band at low energies is clearly separated from the p-band by a bandgap. It indicates that the created potential confines the excited states and realizes the physics discussed in Fig. 1. More importantly, the p-band is split into two sub-bands [as seen also in momentum space, Fig. 2(d)] corresponding to the bonding (in-phase) and anti-bonding (out-of-phase) coupling between the lattice sites (in analogy to electron orbitals in molecules). Despite the small value of the energy gap between the two p-bands, it is larger than the linewidths, allowing us to directly identify the localized states at the edges of the SSH chain. The energies of these states lie inside the p-band gap, as indicated by the arrows in Fig. 3. The spectral cross sections in the bulk (i.e., the middle) and at the edge of the chain are presented in Figs. 2(c) and 2(d), where the shaded areas present the result of fitting the spectrum with Lorentzian lines. Existence of the in-gap edge modes confirmed by these measurements is a signature of a topological phase of the SSH lattice [14,15,34,46]. We note that the occupation of all bands is not spatially homogeneous, as the sample is characterized with an intrinsic

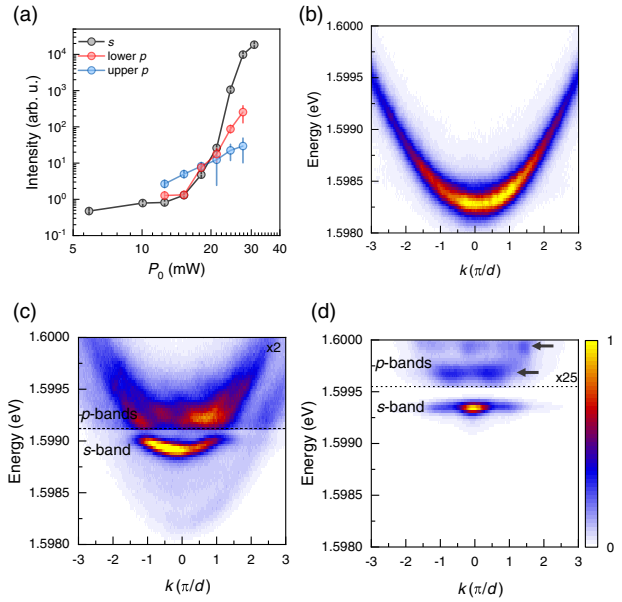

Fig. 2. Power-dependent measurements in momentum space for the $N = 6$ chain. (a) Power-dependent intensity extracted from momentum space at $k = 0$ for the s-band and at $k = \pi/d$ for p-bands. (b) Single-particle polariton dispersion measured below the condensation threshold at $P_0 \approx 6.0$ mW, where the optically induced potential is negligible. (c) Polariton dispersion slightly above the condensation threshold $P_0 \approx 15.3$ mW; s-band and p-bands are indicated. The bandgap between the s- and p-bands is clearly visible. (d) Polariton dispersion above the condensation threshold $P_0 \approx 28$ mW. Arrows indicate the condensate at the s-band and the two upper p-band modes. The upper part of the image with the weak p-band signal is enhanced for clarity. A bandgap between p-bands is well resolved.

linear energy gradient due to the spatially varying thickness of the cavity, oriented antidiagonally with respect to the x axis in the presented data. This effect is captured in our simulations of the full open-dissipative mean-field model [see Methods, Section 2.B, Eq. (4)], with the results presented in Fig. 3(b), showing an excellent agreement with the experimental observations. We emphasize that the simulations are based on experimentally determined parameters of the sample. The energy gradient does not change the topology of the system, as the polariton states at the individual lattice sites are hybridized, which is reflected in the opening of the bandgap of the p-modes. Moreover, the effect of the potential gradient is more pronounced for the s-band than for the p-bands, as seen in Figs. 3(a) and 3(b). This is because the s-states are confined more tightly than p-states in a single trap, and thus the tunneling between the sites is much weaker for s-states. As a result, they do not hybridize in this zigzag configuration, and each lattice site is characterized by a slightly different energy. On the other hand, p-states at each lattice site lie at higher energies and have a larger spatial extent, resulting in enhanced coupling between these states. The effect of band formation only at higher order states has been observed previously in microfabricated structures [47,48]. This is why we focus on the p-band, which is hybridized and shows a well-resolved topologically nontrivial bandgap [Fig. 3(c)], ensuring the realization of the orbital SSH model.

The spatial distribution of the exciton-polariton density in the chain is obtained by real-space spectral tomography, which enables selective real-space imaging of the polariton emission intensity at a given energy (see Methods). The experimental results are presented in Figs. 3(e), 3(g), and 3(i) together with the results of numerical modeling of Eq. (4) in Figs. 3(f), 3(h), and 3(j). The lower p-band shows a characteristic spatial distribution of a bonding state, where the p-modes from neighboring traps overlap [Figs. 3(i) and 3(j)]. The upper p-band shows an antibonding character with pronounced density dips between the traps, indicative of the nodes in the probability density distribution [Figs. 3(e) and 3(f)]. Finally, the edge states are composed of an antidiagonal p-mode configuration forming the topologically nontrivial realization of the SSH model [Figs. 3(g) and 3(h)].

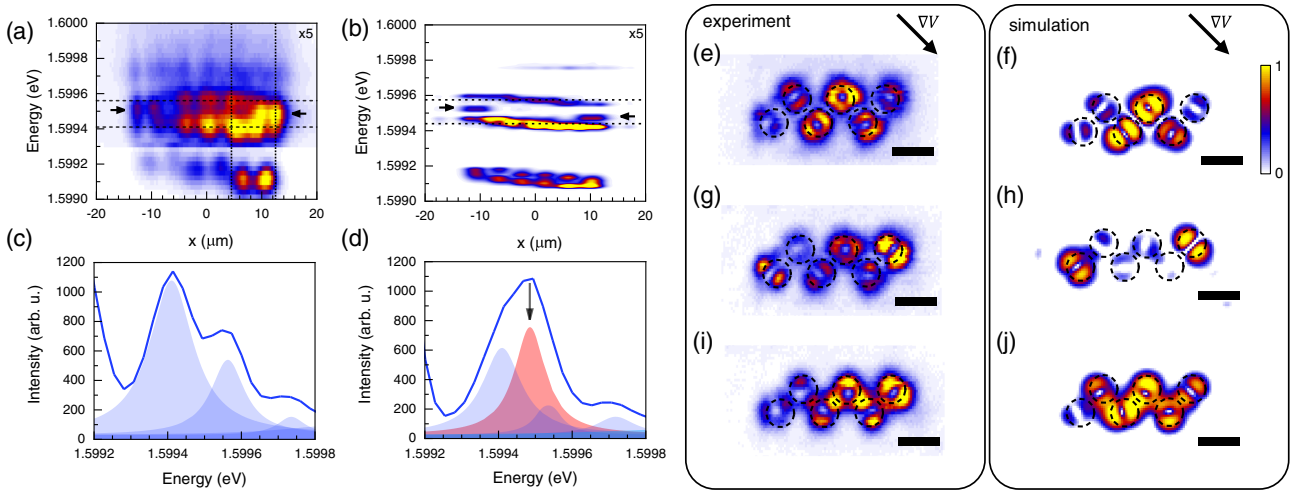

Fig. 3. Position-resolved spectrum and density distribution of exciton polaritons in the SSH chain. (a) Experimentally measured spectrum along the chain with $N = 6$ sites, integrated over the orthogonal (y) direction. (b) Corresponding spectrum obtained by numerical simulations of the mean-field open-dissipative model, Eq. (4) in Methods. Dashed horizontal lines indicate the p-bands and the bandgap. The p- and d-band signals are enhanced 5×, as indicated in the figures. (c), (d) Experimental spectrum measured at a position (c) within the chain, and (d) at the edge of the chain [positions are indicated by vertical dotted lines in (a)]. Shaded areas represent the result of fitting with Lorentzian lines. p-band and d-band peaks are in semitransparent blue, and the edge mode peak is colored in semitransparent red. (e)–(i) Experimental images of the exciton-polariton emission corresponding to spatial density distributions taken at the energies of the (e) upper p-band, (g) edge states (middle of the bandgap), and (i) lower p-band. (f)–(j) Density distributions obtained by numerical simulations of the model Eq. (4) corresponding to (e)–(i). The scale bar corresponds to 10 μm, and the direction of the energy gradient in the sample is indicated with an arrow.

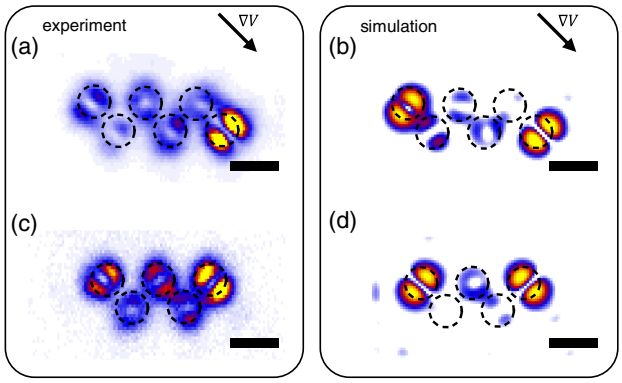

Fig. 4. Topological edge states in different lattice realizations. (a), (c) Experimental spatial density distributions of the edge state for a (a) chain of $N = 6$ sites with a different orientation compared to the chain in Fig. 3 and (c) chain of $N = 5$ sites. (b), (d) Results of numerical simulations of the model Eq. (4) corresponding to the cases in (a) and (c). The scale bar corresponds to 10 μm, and the direction of the energy gradient is indicated with an arrow.

To test the robustness of the topologically protected edge states, we imprinted different chains at different positions on the sample with similar detunings. The edge state for the $N = 6$ chain, similar to that in Fig. 3, but with a different orientation with respect to the energy gradient, is presented in Fig. 4(a) with the corresponding numerical simulation shown in Fig. 4(b). For this orientation, the diagonal p-mode configuration is the topologically nontrivial one. Similar to the $N = 6$ case, the orbital SSH model with an odd number of sites supports two edge states; however, each edge state comes from a different p-mode configuration [14,15,34]. This is clearly seen in our experimental data for a chain with $N = 5$ sites, presented in Fig. 4(c), in agreement with simulations in Fig. 4(d). These results demonstrate the insensitivity of the all-optical realization of the orbital SSH model to the orientation of the energy gradient and local disorder of the sample.

To demonstrate an optically driven topological phase transition in our system, we modified the topology of the $N = 6$ chain by changing the ratio between the tunneling amplitudes from $t_A/t_D > 1$ to $t_A/t_D < 1$ in the $N = 6$ chain. The coupling between the nearest-neighbor sites depends on the potential barrier height as well as on the distance between the traps [49]. Therefore, we increase the coupling t_A or t_D by reducing the trap separations in A or D directions, while keeping all other parameters constant. Importantly, this changes the topology in the s-band as well. Staggering of the couplings in the chain improves coupling between s-states, and one observes a smaller influence of the energy gradient and hybridization in this band.

In this way, we modified the SSH Hamiltonian for p_A configuration. Figures 5(a) and 5(b) present the intensity distribution of the laser excitation reflected from the sample for the chains of modified dimerizations. The chain maintaining the topological phase is presented in Fig. 5(a), and the chain in the trivial phase is shown in Fig. 5(b). In both cases, the lattice constant in one of the directions was reduced by 20% compared to the case presented in Fig. 3. The measured real-space spectra for these geometries are shown in Figs. 5(c) and 5(d). One observes an increase in the topological and trivial bandgaps between the p-bands in comparison to the unmodified chain: $\Delta E_{\text{topo}} = 174 \pm 10$ μeV for $d_D/d_A = 0.8$ and $\Delta E_{\text{triv}} = 218 \pm 8$ μeV for $d_D/d_A = 1.25$ in comparison to $\Delta E_{\text{topo}} = 151 \pm 9$ μeV for $d_D/d_A = 1.0$, in Fig. 3(a). The larger values for the modified chains are a direct manifestation of the control over the tunneling amplitudes, as the bandgap in the SSH model is proportional to $|t_D - t_A|$ (full set of values is presented in Supplement 1). The geometrical modification leading to the change of tunneling amplitudes influences the s-band as well,

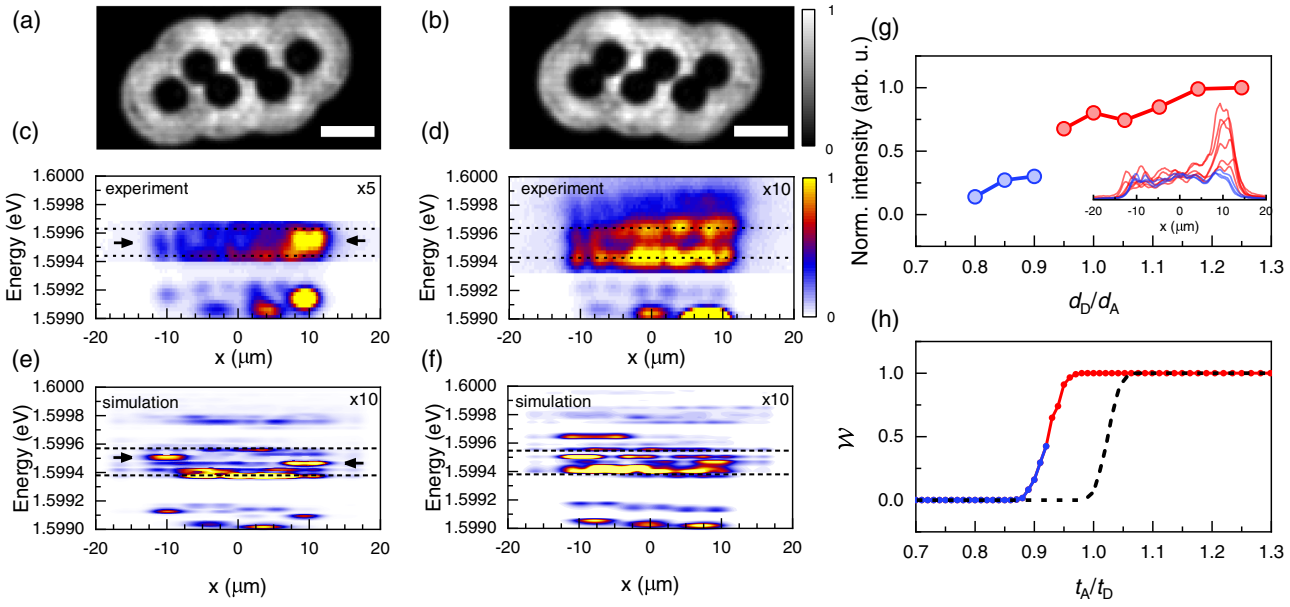

Fig. 5. Measurement of the topological phase transition in SSH chains. (a), (b) Spatial distributions of the excitation intensity reflected from the sample for the modified chains in the (a) topological and (b) trivial phases. The scale bar corresponds to 10 μm. (c), (d) Experimental spectra corresponding to the cases presented in (a), (b). (e), (f) Numerically computed spectra corresponding to the experimental measurements in (c), (d). The p- and d-band signals are multiplied, as indicated in (c)–(f). (g) Intensity of the exciton-polariton edge state at the right end of the modified chains as a function of d_D/d_A. Inset shows the intensity distributions measured in the middle of the p-band gap. (h) Winding number $\mathcal{W}$ calculated from the tight-binding Hamiltonian, including the energy gradient and disorder [see Methods, Eqs. (1)–(3)], as a function of t_A/t_D. The trivial phase is colored in blue, and the topological phase is colored in red in (g), (h). Dashed line in (h) corresponds to the winding number calculated in the case without the potential gradient.

which is now clearly split, and the signatures of edge modes are visible in Fig. 5(c). The asymmetry of the p-band gap values is caused by the energy gradient, which influences the sensitivity of t_A and t_D to the trap separation parameter. Additional input to the tunneling amplitudes comes from the intrinsic TE-TM splitting and weak birefringence of the sample [21,50].

The cavity gradient influences mostly the occupation of the topological edge states in the measured spectrum in Fig. 5(c), with one of the edge states dominating the spectrum. On the other hand, the spectrum in Fig. 5(d) shows no signatures of the edge states, as expected for a topological phase transition to a trivial configuration with $\mathcal{W} = 0$.

The flexibility of our all-optical potential allows us to tune the lattice geometry parameters continuously. Thus, we performed a series of measurements to pinpoint the topological phase transition in the chain. Direct measurement of the winding number $\mathcal{W}$ is challenging in our experimental configuration [51]. Instead, we measure the intensity distribution at the mid-gap and observe the appearance of edge states as a signature of the topological phase [see Fig. 5(g)]. The transition to a trivial state occurs around $d_D/d_A \approx 0.9 - 0.95$, where we observe an abrupt change in the intensity at the edge of the chain [there is a clear asymmetry in the edge modes' occupations for all realizations; see inset in Fig. 5(g)]. We reproduce this observation by calculating the winding number in the tight-binding Hamiltonian, including the potential gradient and random disorder, Eqs. (1) and (3). The disorder, inevitably present in experiments, softens the transition threshold. On the other hand, the energy gradient moves the phase transition away from the point $t_A/t_D = 1$ [Fig. 5(h)], as observed in the experiment. We highlight that the all-optical generation of the lattice could also enable exploration of the intentionally designed disorder and higher winding numbers in staggered zigzag chains [52].

4. CONCLUSION

To summarize, we have demonstrated an all-optically driven topological phase transition in a fully reconfigurable optically induced orbital SSH lattice created in an open-dissipative exciton-polariton system. The transition is controlled by fine-tuning the strength of tunneling between the lattice sites. We emphasize that implementing this kind of control would typically require fabrication of many different samples with different implementations of lattice geometries. Moreover, we have demonstrated the robust topologically protected edge states in a regime where exciton polaritons are condensed and nonlinear (density-dependent) effects could begin to play a role [53,54].

Our realization of the topologically protected edge states depends on the Q-factor of the sample, as the bandgaps are much smaller than those obtained in microfabricated samples [14,15,34,51]. Hence, improved polariton linewidths (lifetimes) [42] are essential to reliably resolve the band structure. Possible ways to improve the measured linewidth-to-bandgap ratio is to use a more photonic detuning (smaller linewidth) or decrease the overlap with the reservoir, by tuning the trap size while maintaining clear energy separation between trapped modes, essentially engineering the gain/loss balance of the system.

We note that the demonstrated method of achieving a topological phase transition in the all-optical realization of a SSH model cannot be straightforwardly extended to other topological phases, e.g., in two dimensions. While generation of 2D lattices by incoherent optical excitation is possible, adding additional resonant control beams allowing for the creation of effective magnetic fields for polaritons would also be essential. Nevertheless, combined with the experimental control of the gain and loss (linewidth) of the trapped polariton condensates [26], our system represents an attractive, flexible platform for further studies of topological effects in a nonlinear and non-Hermitian hybrid photonic system. For example, the nonlinear interactions of polaritons have been predicted to induce topological Chern insulator type states, either in part, by emulating a magnetic field that can be supplemented by spin–orbit coupling [55,56], or fully, by also emulating spin–orbit coupling [5,57]. Nonlinearity also has implications for the propagation of polaritons in topological modes, where they form solitons [53,58–60] and are predicted to exhibit bistability [61]. While the advantage of topological modes is their isolation (in both energy, where they exist in a bandgap, and space, where they are well localized), this can also be a limitation if one wants to deliberately couple them to other modes in the system. Again, nonlinearity offers a possible solution, where the transfer of signals between localized topological states via polariton edge modes has been predicted by making use of polariton parametric scattering [62].

The combination of topological and non-Hermitian features of polaritons sets the foundation for realization of topological polariton lasers [34,63,64]. It could also enable the observation of non-reciprocal behavior and topological non-Hermitian skin effects [65], where all states of a lattice become localized at one edge. The ability to control the topological properties of polaritons with an external optical field suggests that one could engineer different effective lattices for different polariton spin components. This could be done by patterning also the polarization of the external driving field, which is predicted to allow a polariton valley Hall effect [66]. Further, the ability to change the incident optical field, as we have done in this work, is promising for the possible dynamic coupling of edge states [67] if it can be arranged on a faster time scale. Finally, the flexibility of the polariton system could allow realization of novel topological effects in hybrid systems, where the unique features of polaritons are combined with intrinsically magnetic materials [68].

Funding. Australian Research Council (CE170100039); Ministry of Education–Singapore (MOE2018-T3-1-002, MOE2019-T2-1-004); Narodowe Centrum Nauki (2018/30/E/ST7/00648); Fundacja na rzecz Nauki Polskiej (START); National Science Foundation (DMR-2004570).

Disclosures. The authors declare no conflicts of interest.

Data Availability. Data underlying the results presented in this paper are not publicly available at this time but may be obtained from the authors upon reasonable request.

Supplemental document. See Supplement 1 for supporting content.

REFERENCES

1. H. Deng, G. Weihs, C. Santori, J. Bloch, and Y. Yamamoto, "Condensation of semiconductor microcavity exciton polaritons," Science **298**, 199–202 (2002).
2. J. Kasprzak, M. Richard, S. Kundermann, A. Baas, P. Jeambrun, J. M. Keeling, F. M. Marchetti, M. H. Szymánska, R. André, J. L. Staehli, V. Savona, P. B. Littlewood, B. Deveaud, and L. S. Dang, "Bose-Einstein condensation of exciton polaritons," Nature **443**, 409–414 (2006).
3. H. Deng, H. Haug, and Y. Yamamoto, "Exciton-polariton Bose-Einstein condensation," Rev. Mod. Phys. **82**, 1489–1537 (2010).
4. T. Byrnes, N. Y. Kim, and Y. Yamamoto, "Exciton-polariton condensates," Nat. Phys. **10**, 803–813 (2014).
5. C. E. Bardyn, T. Karzig, G. Refael, and T. C. Liew, "Chiral Bogoliubov excitations in nonlinear bosonic systems," Phys. Rev. B **93**, 20502 (2016).

6. D. Leykam and Y. D. Chong, "Edge solitons in nonlinear-photonic topological insulators," Phys. Rev. Lett. **117**, 143901 (2016).
7. T. Ozawa, H. M. Price, A. Amo, N. Goldman, M. Hafezi, L. Lu, M. C. Rechtsman, D. Schuster, J. Simon, O. Zilberberg, and I. Carusotto, "Topological photonics," Rev. Mod. Phys. **91**, 15006 (2019).
8. F. D. Haldane and S. Raghu, "Possible realization of directional optical waveguides in photonic crystals with broken time-reversal symmetry," Phys. Rev. Lett. **100**, 013904 (2008).
9. A. B. Khanikaev, S. Hossein Mousavi, W. K. Tse, M. Kargarian, A. H. MacDonald, and G. Shvets, "Photonic topological insulators," Nat. Mater. **12**, 233–239 (2013).
10. S. Klembt, T. H. Harder, O. A. Egorov, K. Winkler, R. Ge, M. A. Bandres, M. Emmerling, L. Worschech, T. C. Liew, M. Segev, C. Schneider, and S. Höfling, "Exciton-polariton topological insulator," Nature **562**, 552–556 (2018).
11. B. Bahari, A. Ndao, F. Valini, A. E. Amili, Y. Fainman, and B. Kante, "Robust non-reciprocal lasing in topological cavities of arbitrary geometries," Science **358**, 636–640 (2017).
12. M. A. Bandres, S. Wittek, G. Harari, M. Parto, J. Ren, M. Segev, D. N. Christodoulides, and M. Khajavikhan, "Topological insulator laser: experiments," Science **359**, eaar4005 (2018).
13. C. Schneider, K. Winkler, M. D. Fraser, M. Kamp, Y. Yamamoto, E. A. Ostrovskaya, S. Höfling, and S. Höfling, "Exciton-polariton trapping and potential landscape engineering," Rep. Prog. Phys. **80**, 016503 (2017).
14. C. E. Whittaker, E. Cancellieri, P. M. Walker, B. Royall, L. E. Tapia Rodriguez, E. Clarke, D. M. Whittaker, H. Schomerus, M. S. Skolnick, and D. N. Krizhanovskii, "Effect of photonic spin-orbit coupling on the topological edge modes of a Su-Schrieffer-Heeger chain," Phys. Rev. B **99**, 081402 (2019).
15. P. St-Jean, V. Goblot, E. Galopin, A. Lemaître, T. Ozawa, L. Le Gratiet, I. Sagnes, J. Bloch, and A. Amo, "Lasing in topological edge states of a one-dimensional lattice," Nat. Photonics **11**, 651–656 (2017).
16. V. G. Sala, D. D. Solnyshkov, I. Carusotto, T. Jacqmin, A. Lemaître, H. Terças, A. Nalitov, M. Abbarchi, E. Galopin, I. Sagnes, J. Bloch, G. Malpuech, and A. Amo, "Spin-orbit coupling for photons and polaritons in microstructures," Phys. Rev. X **5**, 011034 (2015).
17. S. Alyatkin, H. Sigurdsson, A. Askitopoulos, J. D. Töpfer, and P. G. Lagoudakis, "Interaction induced point scatterer lattices and flat band condensation of exciton-polaritons," arXiv:2007.02807 (2020).
18. M. I. Shalaev, W. Walasik, and N. M. Litchinitser, "Optically tunable topological photonic crystal," Optica **6**, 839–844 (2019).
19. D. Leykam, S. Mittal, M. Hafezi, and Y. D. Chong, "Reconfigurable topological phases in next-nearest-neighbor coupled resonator lattices," Phys. Rev. Lett. **121**, 23901 (2018).
20. Z. A. Kudyshev, A. V. Kildishev, A. Boltasseva, and V. M. Shalaev, "Photonic topological phase transition on demand," Nanophotonics **8**, 1349–1356 (2019).
21. R. Su, S. Ghosh, T. C. H. Liew, and Q. Xiong, "Optical control of topological polariton phase in a perovskite lattice," Sci. Adv. **7**, eabf8049 (2020).
22. E. A. Cerda-Méndez, D. N. Krizhanovskii, M. Wouters, R. Bradley, K. Biermann, K. Guda, R. Hey, P. V. Santos, D. Sarkar, and M. S. Skolnick, "Polariton condensation in dynamic acoustic lattices," Phys. Rev. Lett. **105**, 116402 (2010).
23. E. A. Cerda-Méndez, D. Sarkar, D. N. Krizhanovskii, S. S. Gavrilov, K. Biermann, M. S. Skolnick, and P. V. Santos, "Exciton-polariton gap solitons in two-dimensional lattices," Phys. Rev. Lett. **111**, 146401 (2013).
24. D. Sanvitto, S. Pigeon, A. Amo, D. Ballarini, M. De Giorgi, I. Carusotto, R. Hivet, F. Pisanello, V. G. Sala, P. S. Guimaraes, R. Houdré, E. Giacobino, C. Ciuti, A. Bramati, and G. Gigli, "All-optical control of the quantum flow of a polariton condensate," Nat. Photonics **5**, 610–614 (2011).
25. A. Askitopoulos, H. Ohadi, A. V. Kavokin, Z. Hatzopoulos, P. G. Savvidis, and P. G. Lagoudakis, "Polariton condensation in an optically induced two-dimensional potential," Phys. Rev. B **88**, 041308 (2013).
26. T. Gao, E. Estrecho, K. Y. Bliokh, T. C. Liew, M. D. Fraser, S. Brodbeck, M. Kamp, C. Schneider, S. Höfling, Y. Yamamoto, F. Nori, Y. S. Kivshar, A. G. Truscott, R. G. Dall, and E. A. Ostrovskaya, "Observation of non-Hermitian degeneracies in a chaotic exciton-polariton billiard," Nature **526**, 554–558 (2015).
27. H. Ohadi, Y. Del Valle-Inclan Redondo, A. J. Ramsay, Z. Hatzopoulos, T. C. Liew, P. R. Eastham, P. G. Savvidis, and J. J. Baumberg, "Synchronization crossover of polariton condensates in weakly disordered lattices," Phys. Rev. B **97**, 195109 (2018).
28. A. Poddubny, A. Miroshnichenko, A. Slobozhanyuk, and Y. Kivshar, "Topological Majorana states in zigzag chains of plasmonic nanoparticles," ACS Photon. **1**, 101–105 (2014).
29. I. S. Sinev, I. S. Mukhin, A. P. Slobozhanyuk, A. N. Poddubny, A. E. Miroshnichenko, A. K. Samusev, and Y. S. Kivshar, "Mapping plasmonic topological states at the nanoscale," Nanoscale **7**, 11904–11908 (2015).
30. A. P. Slobozhanyuk, A. N. Poddubny, A. E. Miroshnichenko, P. A. Belov, and Y. S. Kivshar, "Subwavelength topological edge states in optically resonant dielectric structures," Phys. Rev. Lett. **114**, 123901 (2015).
31. S. Kruk, A. Slobozhanyuk, D. Denkova, A. Poddubny, I. Kravchenko, A. Miroshnichenko, D. Neshev, and Y. Kivshar, "Edge states and topological phase transitions in chains of dielectric nanoparticles," Small **13**, 1603190 (2017).
32. S. Kruk, A. Poddubny, D. Smirnova, L. Wang, A. Slobozhanyuk, A. Shorokhov, I. Kravchenko, B. Luther-Davies, and Y. Kivshar, "Nonlinear light generation in topological nanostructures," Nat. Nanotechnol. **14**, 126–130 (2019).
33. A. Tripathi, S. Kruk, Y. Shang, J. Zhou, I. Kravchenko, D. Jin, and Y. Kivshar, "Topological nanophotonics for photoluminescence control," Nanophotonics **10**, 435–441 (2021).
34. T. H. Harder, M. Sun, O. A. Egorov, I. Vakulchyk, J. Beierlein, P. Gagel, M. Emmerling, C. Schneider, U. Peschel, I. G. Savenko, S. Klembt, and S. Höfling, "Coherent topological polariton laser," ACS Photon. **8**, 1377–1384 (2021).
35. L. Pickup, H. Sigurdsson, J. Ruostekoski, and P. G. Lagoudakis, "Synthetic band-structure engineering in polariton crystals with non-Hermitian topological phases," Nat. Commun. **11**, 4431 (2020).
36. N. G. Berloff, M. Silva, K. Kalinin, A. Askitopoulos, J. D. Töpfer, P. Cilibrizzi, W. Langbein, and P. G. Lagoudakis, "Realizing the classical XY Hamiltonian in polariton simulators," Nat. Mater. **16**, 1120–1126 (2017).
37. K. Orfanakis, A. F. Tzortzakakis, D. Petrosyan, P. G. Savvidis, and H. Ohadi, "Ultralong temporal coherence in optically trapped exciton-polariton condensates," Phys. Rev. B **103**, 235313 (2021).
38. E. Estrecho, T. Gao, N. Bobrovska, D. Comber-Todd, M. D. Fraser, M. Steger, K. West, L. N. Pfeiffer, J. Levinsen, M. M. Parish, T. C. H. Liew, M. Matuszewski, D. W. Snoke, A. G. Truscott, and E. A. Ostrovskaya, "Direct measurement of polariton-polariton interaction strength in the Thomas-Fermi regime of exciton-polariton condensation," Phys. Rev. B **100**, 035306 (2019).
39. W. P. Su, J. R. Schrieffer, and A. J. Heeger, "Solitons in polyacetylene," Phys. Rev. Lett. **42**, 1698 (1979).
40. C. Han, M. Lee, S. Callard, C. Seassal, and H. Jeon, "Lasing at topological edge states in a photonic crystal L3 nanocavity dimer array," Light Sci. Appl. **8**, 40 (2019).
41. Y. Ota, R. Katsumi, K. Watanabe, S. Iwamoto, and Y. Arakawa, "Topological photonic crystal nanocavity laser," Commun. Phys. **1**, 4–6 (2018).
42. M. Steger, C. Gautham, D. W. Snoke, L. Pfeiffer, and K. West, "Slow reflection and two-photon generation of microcavity exciton–polaritons," Optica **2**, 1–5 (2015).
43. M. Pieczarka, E. Estrecho, M. Boozarjmehr, O. Bleu, M. Steger, K. West, L. N. Pfeiffer, D. W. Snoke, J. Levinsen, M. M. Parish, A. G. Truscott, and E. A. Ostrovskaya, "Observation of quantum depletion in a non-equilibrium exciton–polariton condensate," Nat. Commun. **11**, 429 (2020).
44. D. Read, T. C. H. Liew, Y. G. Rubo, and A. V. Kavokin, "Stochastic polarization formation in exciton-polariton Bose-Einstein condensates," Phys. Rev. B **80**, 195309 (2009).
45. M. Wouters, T. C. H. Liew, and V. Savona, "Energy relaxation in one-dimensional polariton condensates," Phys. Rev. B **82**, 245315 (2010).
46. M. Z. Hasan and C. L. Kane, "Colloquium: topological insulators," Rev. Mod. Phys. **82**, 3045–3067 (2010).
47. T. Gao, E. Estrecho, G. Li, O. A. Egorov, X. Ma, K. Winkler, M. Kamp, C. Schneider, S. Höfling, A. G. Truscott, and E. A. Ostrovskaya, "Talbot effect for exciton polaritons," Phys. Rev. Lett. **117**, 097403 (2016).
48. A. Mischok, R. Brückner, H. Fröb, V. G. Lyssenko, K. Leo, and A. A. Zakhidov, "Control of lasing from Bloch states in microcavity photonic wires via selective excitation and gain," Phys. Rev. Appl. **3**, 064016 (2015).
49. M. Galbiati, L. Ferrier, D. D. Solnyshkov, D. Tanese, E. Wertz, A. Amo, M. Abbarchi, P. Senellart, I. Sagnes, A. Lemaître, E. Galopin, G. Malpuech,

and J. Bloch, "Polariton condensation in photonic molecules," Phys. Rev. Lett. **108**, 126403 (2012).
50. D. Biegańska, M. Pieczarka, E. Estrecho, M. Steger, D. W. Snoke, K. West, L. N. Pfeiffer, M. Syperek, A. G. Truscott, and E. A. Ostrovskaya, "Collective excitations of exciton-polariton condensates in a synthetic gauge field," arXiv:2011.13290 (2020).
51. P. St-Jean, A. Dauphin, P. Massignan, B. Real, O. Jamadi, M. Milicevic, A. Lematre, A. Harouri, L. Le Gratiet, I. Sagnes, S. Ravets, J. Bloch, and A. Amo, "Measuring topological invariants in a polaritonic analog of graphene," Phys. Rev. Lett. **126**, 127403 (2021).
52. L. Lin, S. Kruk, Y. Ke, C. Lee, and Y. Kivshar, "Topological states in disordered arrays of dielectric nanoparticles," Phys. Rev. Res. **2**, 043233 (2020).
53. N. Pernet, P. St-Jean, D. D. Solnyshkov, G. Malpuech, N. C. Zambon, B. Real, O. Jamadi, A. Lemaître, M. Morassi, L. L. Gratiet, T. Baptiste, A. Harouri, I. Sagnes, A. Amo, S. Ravets, and J. Bloch, "Topological gap solitons in a 1D non-Hermitian lattice," arXiv:2101.01038 (2021).
54. P. Comaron, V. Shahnazaryan, W. Brzezicki, T. Hyart, and M. Matuszewski, "Non-Hermitian topological end-mode lasing in polariton systems," Phys. Rev. Res. **2**, 022051 (2020).
55. O. Bleu, D. D. Solnyshkov, and G. Malpuech, "Full optical control of topological transitions in polariton Chern insulator analog," arXiv:1606.07410 (2016).
56. H. Sigurdsson, Y. S. Krivosenko, I. V. Iorsh, I. A. Shelykh, and A. V. Nalitov, "Spontaneous topological transitions in a honeycomb lattice of exciton-polariton condensates due to spin bifurcations," Phys. Rev. B **100**, 235444 (2019).
57. H. Sigurdsson, G. Li, and T. C. H. Liew, "Spontaneous and superfluid chiral edge states in exciton-polariton condensates," Phys. Rev. B **96**, 115453 (2017).
58. Y. V. Kartashov and D. V. Skryabin, "Modulational instability and solitary waves in polariton topological insulators," Optica **3**, 1228–1236 (2016).
59. D. R. Gulevich, D. Yudin, D. V. Skryabin, I. V. Iorsh, and I. A. Shelykh, "Exploring nonlinear topological states of matter with exciton-polaritons: edge solitons in Kagome lattice," Sci. Rep. **7**, 1780 (2017).
60. W. Zhang, X. Chen, Y. V. Kartashov, V. V. Konotop, and F. Ye, "Coupling of edge states and topological Bragg solitons," Phys. Rev. Lett. **123**, 254103 (2019).
61. Y. V. Kartashov and D. V. Skryabin, "Bistable topological insulator with exciton-polaritons," Phys. Rev. Lett. **119**, 253904 (2017).
62. R. Banerjee, S. Mandal, and T. C. H. Liew, "Coupling between exciton-polariton corner modes through edge states," Phys. Rev. Lett. **124**, 063901 (2020).
63. Y. V. Kartashov and D. V. Skryabin, "Two-dimensional topological polariton laser," Phys. Rev. Lett. **122**, 083902 (2019).
64. M. Dusel, S. Betzold, T. H. Harder, M. Emmerling, J. Ohmer, U. Fischer, R. Thomale, C. Schneider, S. Höfling, and S. Klembt, "Room temperature topological polariton laser in an organic lattice," arXiv:2012.11945 (2020).
65. S. Mandal, R. Banerjee, E. A. Ostrovskaya, and T. C. H. Liew, "Nonreciprocal transport of exciton polaritons in a non-Hermitian chain," Phys. Rev. Lett. **125**, 123902 (2020).
66. R. Banerjee, S. Mandal, and T. C. H. Liew, "Optically induced topological spin-valley Hall effect for exciton polaritons," Phys. Rev. B **103**, L201406 (2021).
67. Y. Zhang, Y. V. Kartashov, Y. Zhang, L. Torner, and D. V. Skryabin, "Resonant edge-state switching in polariton topological insulators," Laser Photon. Rev. **12**, 1700348 (2018).
68. M. Sun, D. Ko, D. Leykam, V. M. Kovalev, and I. G. Savenko, "Exciton-polariton topological insulator with an array of magnetic dots," Phys. Rev. Appl. **12**, 064028 (2019).